

Geometrical interpretation of fMRI-guided MEG/EEG inverse estimates

Seppo P. Ahlfors^{a,*} and Gregory V. Simpson^b

^aMGH/MIT/HMS Athinoula A. Martinos Center for Biomedical Imaging, Massachusetts General Hospital, Harvard Medical School, Charlestown, MA 02129, USA

^bDynamic Neuroimaging Laboratory, Department of Radiology, University of California, San Francisco, San Francisco, CA 94143, USA

Received 28 August 2003; revised 18 December 2003; accepted 23 December 2003

Magneto- and electroencephalography (MEG/EEG) and functional magnetic resonance imaging (fMRI) provide complementary information about the functional organization of the human brain. An important advantage of MEG/EEG is the millisecond time resolution in detecting electrical activity in the cerebral cortex. The interpretation of MEG/EEG signals, however, is limited by the difficulty of determining the spatial distribution of the neural activity. Functional MRI can help in the MEG/EEG source analysis by suggesting likely locations of activity. We present a geometric interpretation of fMRI-guided inverse solutions in which the MEG/EEG source estimate minimizes a distance to a subspace defined by the fMRI data. In this subspace regularization (SSR) approach, the fMRI bias does not assume preferred amplitudes for MEG/EEG sources, only locations. Characteristic dependence of the source estimates on the regularization parameters is illustrated with simulations. When the fMRI locations match the true MEG/EEG source locations, they serve to bias the underdetermined MEG/EEG inverse solution toward the fMRI loci. Importantly, when the fMRI loci do not match the true MEG/EEG loci, the solution is insensitive to those fMRI loci.

© 2004 Elsevier Inc. All rights reserved.

Keywords: Magnetoencephalography; Electroencephalography; Functional magnetic resonance imaging; Subspace regularization

Introduction

The functional organization of the human brain can be readily studied with a variety of noninvasive imaging tools. Magneto- and electroencephalography (MEG/EEG) are techniques of recording extracranial magnetic field or scalp potential, respectively, generated by electrophysiologic events in the brain (Cohen and Halgren, 2003; Gevins et al., 1995; Hämäläinen et al., 1993). MEG and EEG can detect activity in the time scale characteristic of communication between neurons, thus providing an important benefit over measures of secondary phenomena such as hemodynamics

recorded using functional magnetic resonance imaging (fMRI), positron emission tomography (PET), or near infrared imaging (NIR). The interpretation of MEG/EEG data, however, is limited by the difficulty of determining the spatial distribution of source currents in the brain. There is no unique solution for this bioelectromagnetic inverse problem (Helmholtz, 1853): To any given solution that is compatible with the measured data, it is always possible to add a “silent” source distribution that does not produce any signal in the sensors.

A reasonably accurate localization of MEG/EEG brain sources, however, can be obtained by incorporating additional information and model assumptions. Often, the brain current sources are modeled with a small number (typically less than 10) of equivalent current dipoles (Scherg and Von Cramon, 1986) or with distributed sources with minimum norm properties (Ahlfors et al., 1992; Dale and Sereno, 1993; Grave de Peralta Menendez et al., 1997; Greenblatt, 1993; Hämäläinen and Ilmoniemi, 1984, 1994; Ioannides, 1993; Jeffs et al., 1987; Pascual-Marqui et al., 1994; Sekihara and Scholz, 1996; Smith et al., 1990). Realistic anatomic information from MRI can be used to constrain the sources to the cortical gray matter (Dale and Sereno, 1993; Fuchs et al., 1999; George et al., 1991; Phillips et al., 2002a; Wang et al., 1992). Many types of data can be used as additional information in the inverse estimation procedures, such as intracranial electrophysiologic data from humans and nonhuman primates, lesion data, and functional imaging data from fMRI, PET, and NIR. For example, hemodynamic data (fMRI and PET) have been used to suggest likely locations for MEG sources (Ahlfors et al., 1999; Dale et al., 2000; George et al., 1995; Heinze et al., 1994; Korvenoja et al., 1999; Liu et al., 1998, 2002; Menon et al., 1997; Simpson et al., 1993, 1995; Snyder et al., 1995; Woldorff et al., 1999; Worden et al., 1996).

It is reasonable to expect a large degree of correspondence between MEG/EEG and fMRI/PET, and a number of good correlations have been found (Beisteiner et al., 1997; FitzGerald et al., 1997; Malonek and Grinvald, 1996; Morioka et al., 1995; Puce, 1995; Sanders et al., 1996). However, the relation between the physiology measured with fMRI/PET and the electrophysiology measured with MEG/EEG is complex (Devor et al., 2003; Logothetis, 2003), and there are reasons to expect mismatches between these measures. Therefore, it is important to allow for the possibility that some of the MEG/EEG sources may be missing in

* Corresponding author. Athinoula A. Martinos Center, Massachusetts General Hospital, Harvard Medical School, 149 13th Street, Mailcode 149-2301, Charlestown, MA 02129. Fax: +1-617-726-7422.

E-mail address: seppo@nmr.mgh.harvard.edu (S.P. Ahlfors).

Available online on ScienceDirect (www.sciencedirect.com).

the fMRI/PET data and vice versa (Ahlfors et al., 1999; Liu et al., 1998). For distributed source models, Liu et al. (1998) presented a method in which fMRI information is incorporated in the a priori source covariance matrix. Their method contained an adjustable parameter that determines the degree of fMRI weighting. The fMRI locations are preferred in the MEG/EEG inverse solutions, without completely excluding the possibility of non-fMRI sources.

We present an alternative formulation based on the perspective provided by the concept of subspace regularization (SSR). Previously, SSR has been applied to electrical impedance tomography (Vauhkonen et al., 1998) and single-trial analysis of event-related potentials (Karjalainen et al., 1999). We propose an SSR approach in which the MEG/EEG source estimate is chosen from the set of those source distributions compatible with the MEG/EEG data such that it minimizes the distance to a subspace defined by the fMRI/PET data. The aim of the present work is to provide insight to the problem of fMRI-guided MEG/EEG inverse estimation by presenting a geometric interpretation of how the prior information influences the solution and to illustrate qualitatively the properties of the solutions as a function of the regularization parameters. For brevity, we talk below about MEG and fMRI, but the approach is applicable to EEG and PET/NIR in place of, or in addition to, MEG and fMRI, respectively.

Methods

Our geometric description of the sub-space-regularized MEG inverse estimation is based on four central concepts: (1) the source space, the elements of which are current distributions in the brain; (2) the lead field subspace S^a , which is determined by the sensitivity patterns of the MEG sensors; (3) the set M of all source distributions that are compatible with the actual recorded MEG data at a given time point; and (4) the subspace S^{fMRI} , which is determined by the fMRI data. The fMRI-guided estimate is obtained by selecting from the set M the source distribution that minimizes a measure of distance to S^{fMRI} .

The source space

The generators of MEG signals are modeled as a distribution of active source currents (primary currents) within the brain. The set of all possible source current distributions is determined by anatomic and physiologic a priori information. This set determines the source space (also known as the current space or the model space).

For continuous current distributions, the source space is infinite dimensional. In the discretized model, the brain volume is divided into a relatively large number (typically hundreds or thousands) of elements, and the net source current within each volume element is represented by an equivalent current dipole (Fig. 1A). If the source orientations are determined by anatomic information, for example, by requiring the current to be perpendicular to the cortical surface segmented from each individual subject's anatomic MRI, one dipole with a fixed orientation is adequate for each volume element (Dale and Sereno, 1993; Fuchs et al., 1999); in general, three orthogonal dipole components are required. If the total number of dipole elements is n (which may be three times the number of volume elements), the source space is n -dimensional and the source distributions, denoted by \mathbf{q} , are vectors with n elements. Solving the discretized inverse problem refers to determining the

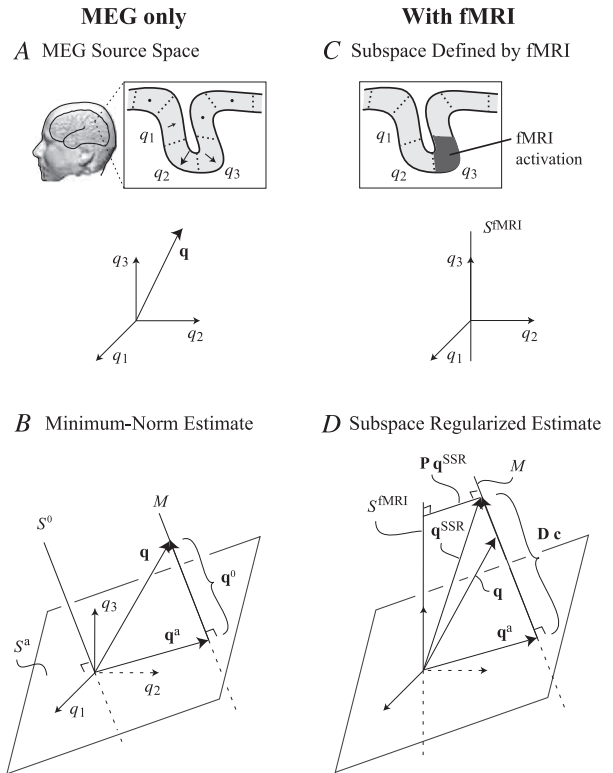


Fig. 1. Geometrical interpretation of subspace regularization in the MEG/EEG source space. (A) The cerebral cortex is divided into source elements q_1, q_2, \dots, q_m , each representing a current dipole with a fixed orientation. These elements correspond to the coordinate axes of an n -dimensional source space. Only three of the n axes are depicted. All source distributions \mathbf{q} are vectors in this space. (B) The source distribution \mathbf{q} is divided into two components: \mathbf{q}^a is a vector in the subspace S^a defined by the sensor lead fields, and \mathbf{q}^0 belongs to the complement S^0 producing no signal in the sensors. M is the set of all vectors whose projection to S^a equals \mathbf{q}^a , thus generating the same MEG/EEG signals. (C) The fMRI activations define another subspace S^{fMRI} . In this example, the fMRI activity occurred at the volume element corresponding to source dipole q_3 . (D) The subspace regularized fMRI-guided solution \mathbf{q}^{SSR} is obtained by choosing the point in M that is closest to S^{fMRI} , minimizing the distance $\|\mathbf{P}\mathbf{q}^{SSR}\|$.

amplitude (as a function of time) of each dipole element on the basis of the measured MEG data.

Note the difference between the “source space” and the “signal space”: the axes of the signal space represent the sensors (a “signal vector” \mathbf{b} has the measured signals b_i as elements) (Glaser and Ruchkin, 1976; Tesche et al., 1995; Uusitalo and Ilmoniemi, 1997) or a linear combination of them corresponding to the highest singular values of the measured data (Greenblatt, 1993; Mosher et al., 1992). The source space involves assumptions about the possible brain sources, whereas the signal space does not.

The lead field subspace

The lead field \mathbf{a}_i describes the sensitivity pattern of the i th MEG sensor (Cuffin and Cohen, 1979). For a source vector \mathbf{q} , the measured signal is $b_i = \mathbf{a}_i^T \mathbf{q} + n_i$, where T denotes the transpose and n_i is noise. In matrix notation,

$$\mathbf{b} = \mathbf{A}\mathbf{q} + \mathbf{n}, \quad (1)$$

where $\mathbf{b} = (b_1, b_2, \dots, b_m)^T$, $\mathbf{n} = (n_1, n_2, \dots, n_m)^T$, and $\mathbf{A} = (\mathbf{a}_1, \mathbf{a}_2, \dots, \mathbf{a}_m)^T$; m is the number of sensors. The matrix \mathbf{A} is often called the forward matrix or the gain matrix.

The lead fields \mathbf{a}_i can also be considered as vectors in the source space, spanning a subspace S^a . Any source distribution \mathbf{q} can be expressed as the sum of two components, one belonging to S^a and one to its orthogonal complement S^0 (Fig. 1B):

$$\mathbf{q} = \mathbf{q}^a + \mathbf{q}^0 \quad (2)$$

The “visible” component \mathbf{q}^a is the orthogonal projection of \mathbf{q} into the lead field subspace S^a (Hämäläinen and Ilmoniemi, 1994). The “silent” component \mathbf{q}^0 is orthogonal to all lead fields, and thus does not produce any signal in the sensors.

The set of sources that match the measured MEG

The nonuniqueness of the inverse problem is manifested by the fact that any vector belonging to the silent subspace S^0 can be added to a given solution without changing the signals measured by the sensors. We denote by M the set of all source distributions that generate a given MEG signal within the limits of noise:

$$M = \{\mathbf{q} \mid \|\mathbf{b} - \mathbf{A}\mathbf{q}\|^2 \leq \eta^2\}, \quad (3)$$

where η^2 is proportional to the noise level (e.g., $\eta^2 = \text{Tr}\mathbf{C}$, the sum of the diagonal elements of the sensor noise covariance matrix \mathbf{C}). M is a cylindrical set (Backus, 1971) such that for any $\mathbf{q} \in M$, the orthogonal projection to the lead field subspace belongs to a hyperellipsoid in S^a . If there is no noise in the measurements, the hyperellipsoid reduces to one point (\mathbf{q}^a), which equals the L_2 minimum norm estimate (MNE) (Hämäläinen and Ilmoniemi, 1994), and M is obtained by translation of S^0 by \mathbf{q}^a (see Fig. 1B).

Regularization can be used to set preferences to solutions within the set M . For example, the solution with minimum L_2 norm is found by minimizing the cost function (Tikhonov and Arsenin, 1977):

$$\arg \min_{\mathbf{q}} [(\mathbf{b} - \mathbf{A}\mathbf{q})^T \mathbf{C}^{-1} (\mathbf{b} - \mathbf{A}\mathbf{q}) + \lambda \mathbf{q}^T \mathbf{q}], \quad (4)$$

where the regularization parameter λ controls the trade-off between the discrepancy between the measured and modeled signal values and the length of the source vector. The larger the regularization parameter λ , the smaller will be the length of the regularized source estimate.

The fMRI-defined subspace and the fMRI-guided source estimate

On the basis of the measured MEG data only, all distributions belonging to M are equally good. One way to set preferences within M is to use fMRI data for additional information about the brain activation. The fMRI-guided estimate is obtained by finding a vector in M that best matches with the fMRI data.

Assuming that the discretization of the MEG source space corresponds to the fMRI voxel size, each voxel containing significant fMRI activity corresponds to one axis (or three axes if no orientation constraint is imposed) of the MEG source space. Each source element corresponding to an fMRI voxel defines a basis vector $\mathbf{e}_k^{\text{fMRI}}$. These vectors span a subspace S^{fMRI} of the source space (Fig. 1C). Any combination of MEG sources (of arbitrary amplitudes) at these locations belongs to S^{fMRI} .

In the SSR approach, a term proportional to the square of the distance $\|\mathbf{P}\mathbf{q}\|$ to the fMRI subspace (Fig. 1D) is added to the cost function. The sub-space-regularized solution \mathbf{q}^{SSR} minimizes the expression:

$$\arg \min_{\mathbf{q}} [(\mathbf{b} - \mathbf{A}\mathbf{q})^T \mathbf{C}^{-1} (\mathbf{b} - \mathbf{A}\mathbf{q}) + \lambda_1 \mathbf{q}^T \mathbf{q} + \lambda_2 \mathbf{q}^T \mathbf{P}\mathbf{q}]. \quad (5)$$

The matrix

$$\mathbf{P} = \mathbf{I} - \sum_k \mathbf{e}_k^{\text{fMRI}} (\mathbf{e}_k^{\text{fMRI}})^T \quad (6)$$

is the projection matrix into the orthogonal complement of S^{fMRI} ; the index k goes over all source elements corresponding to active fMRI voxels; \mathbf{I} is an identity matrix. Note that $\mathbf{P}^2 = \mathbf{P}^T = \mathbf{P}$. The two regularization parameters, λ_1 and λ_2 , determine the relative weight assigned to the norm of the source vector and the discrepancy from fMRI. Since $\mathbf{e}_k^{\text{fMRI}}$ corresponds to axes of the source space, \mathbf{P} is a diagonal matrix with elements being either one or zero:

$$\mathbf{P} = \text{diag}(1 - \delta_l), \quad (7)$$

where $\delta_l = 1$ for source elements corresponding to active fMRI voxels, and $\delta_l = 0$ otherwise.

The cost function in Eq. (5) can be rearranged as

$$\arg \min_{\mathbf{q}} [(\mathbf{b} - \mathbf{A}\mathbf{q})^T \mathbf{C}^{-1} (\mathbf{b} - \mathbf{A}\mathbf{q}) + \mathbf{q}^T \mathbf{R}^{-1} \mathbf{q}], \quad (8)$$

where

$$\mathbf{R}^{-1} = \lambda_1 \mathbf{I} + \lambda_2 \mathbf{P} = \text{diag}[\lambda_1 + \lambda_2(1 - \delta_l)]. \quad (9)$$

The solution is (Tarantola, 1987)

$$\mathbf{q}^{\text{SSR}} = \mathbf{R}\mathbf{A}^T (\mathbf{A}\mathbf{R}\mathbf{A}^T + \mathbf{C})^{-1} \mathbf{b}. \quad (10)$$

Explicit minimization of the distance to the fMRI subspace

To further illuminate the geometric interpretation of the fMRI-guided estimate, we derive a formula for the noiseless case for solving explicitly the vector belonging to the set of possible solutions M that minimize the distance to S^{fMRI} . The estimate is constructed by adding to \mathbf{q}^a , a vector $\mathbf{q}^0 = \mathbf{D}\mathbf{c}$ that belongs to the silent subspace S^0 :

$$\mathbf{q}^{\text{SSR}} = \mathbf{q}^a + \mathbf{D}\mathbf{c}. \quad (11)$$

The columns of the matrix \mathbf{D} contain a set of orthonormal basis vectors of S^0 . The coefficients $\mathbf{c} = (c_1, c_2, \dots)$ are chosen so that the new estimate is either in the fMRI subspace S^{fMRI} or as close to it as possible (Fig. 1C). The squared distance from \mathbf{q}^{SSR} to S^{fMRI} to be minimized is

$$\|\mathbf{P}\mathbf{q}^{\text{SSR}}\|^2 = ((\mathbf{q}^a)^T + \mathbf{c}^T \mathbf{D}^T) \mathbf{P} (\mathbf{q}^a + \mathbf{D}\mathbf{c}) \quad (12)$$

Solving \mathbf{c} by requiring that the derivative with respect to all c_i to be zero and inserting it in Eq. (11), we obtain the fMRI-guided estimate

$$\mathbf{q}^{\text{SSR}} = [\mathbf{I} - \mathbf{D}(\mathbf{D}^T \mathbf{P} \mathbf{D})^\dagger \mathbf{D}^T \mathbf{P}] \mathbf{q}^a, \quad (13)$$

where \dagger indicates pseudoinverse. In Appendix B, we present an example with only three sources and two sensors to visualize the

geometric interpretation of Eq. (13). There are three special cases where the fMRI does not affect the solution ($\mathbf{q}^{\text{SSR}} = \mathbf{q}^a$). (1) If $S^a \subset S^{\text{fMRI}}$, that is, the fMRI subspace includes the whole MEG-visible subspace, then \mathbf{q}^a matches the fMRI data and there is no benefit from an added silent component; in this case, $\mathbf{P}\mathbf{q}^a = 0$ in Eqs. (12) and (13). (2) If $S^{\text{fMRI}} \subset S^a$, then the fMRI subspace is always orthogonal to S^0 and an additional MEG-invisible component does not affect the distance to S^{fMRI} ; in this case, $\mathbf{D}^T\mathbf{P}\mathbf{q}^a = 0$. (3) In the unlikely case of $S^{\text{fMRI}} \perp S^a$, all fMRI voxels would be invisible to MEG and fMRI cannot provide bias to the MEG solution; again, $\mathbf{D}^T\mathbf{P}\mathbf{q}^a = 0$.

Here, it was assumed that there is no noise in the measured signals. Eq. (13), however, can also be applied for noisy data, but taking \mathbf{q}^a to be the MNE. Thus, instead of minimizing the distance to S^{fMRI} within the full cylinder set M (as in Eq. (5)), the MNE within the hyperellipsoid in S^a is computed first, and then a silent component is added such that $\|\mathbf{P}\mathbf{q}\|^2$ is minimized.

Simulations

The performance of the proposed method was examined with numerical simulations. Extensive quantitative simulations of the cross-talk and point-spread functions of fMRI-guided MEG inverse estimates in a realistic head model have been presented by Liu et al. (1998). Since the SSR approach is closely related to their method (see Appendix A), we do not reproduce those types of

simulations here. Instead, we illustrate qualitatively the effect of regularization in a simplified geometry for matching and non-matching fMRI and MEG locations.

To illustrate the lateral spread of activity in the estimates, a planar source configuration was chosen, consisting a grid of 11×11 source locations on the xy -plane, separated by 10 mm. At each location, there were two tangential, mutually orthogonal current dipoles. Thus, the dimension of the source space (the total number of source elements) was $2 \times 11 \times 11 = 242$. The sensor configuration consisted either $12 \times 12 = 144$ or $7 \times 7 = 49$ pointlike magnetometers, measuring the normal component B_z of the magnetic field. The sensors were located on a plane $z_s = 30$ mm above the sources. Distance between adjacent sensors was either 10 mm (the 12×12 sensor grid) or 20 mm (7×7 grid). The volume conductor was assumed to be horizontally layered; thus, the simulated magnetic signal in a sensor at $(x_s, y_s, z_s)^T$ generated by a source $(Q_x, Q_y, 0)^T$ at $(x_Q, y_Q, 0)^T$ was (4):

$$B_z = [Q_x(y_s - y_Q) - Q_y(x_s - x_Q)] / [(x_s - x_Q)^2 + (y_s - y_Q)^2 + z_s^2]^{3/2} \quad (14)$$

The lead field vectors \mathbf{a}_i were calculated by applying unit sources to this formula.

Simulated measurements were created using the source distribution shown in Fig. 2A, with two dipoles located at $(x_Q, y_Q) = (4, 5)$ and $(9, 6)$ [cm] and with dipole moments $(Q_x, Q_y) = (0, 4)$ and $(-4, 0)$, respectively. Properties of the MEG inverse estimate in the

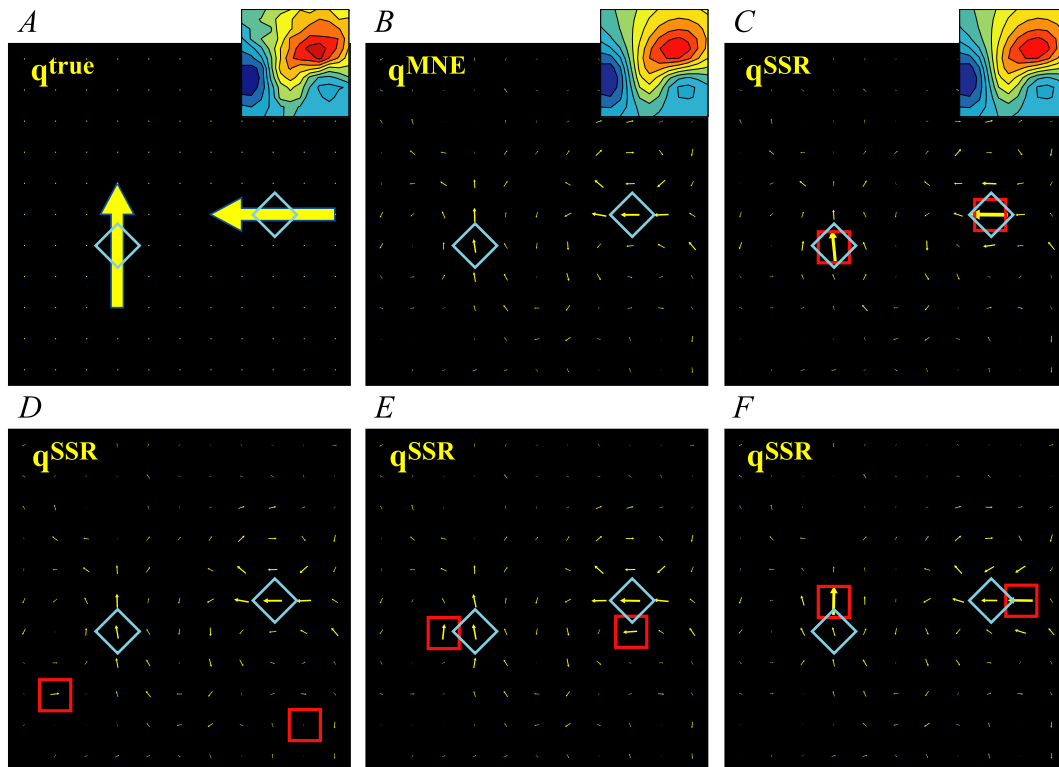


Fig. 2. Source estimates for simulated MEG data. (A) Simulated source configuration \mathbf{q} consisting two active elements on the xy -plane. The arrows indicate the magnitude and orientation of the source elements. The blue diamonds indicate the locations of the true sources. Isocontour map of the simulated magnetic field B_z as measured by a 12×12 grid of sensors is shown in the upper right corner. (B) The minimum norm estimate \mathbf{q}^{MNE} (without fMRI information). The small arrows represent the estimated source distribution. The field pattern generated by this source distribution is shown at upper right. (C) The fMRI-guided subspace-regularized source estimate \mathbf{q}^{SSR} . The red squares depict the locations of fMRI activity, which in this case match the MEG locations. (D–F) The fMRI-guided estimate \mathbf{q}^{SSR} in the presence of simultaneous false-positive and false-negative (missing) fMRI. The fMRI loci are either far from the MEG sources (D), displaced sideways with respect to (E), or along (F) the direction of the dipole moment.

presence of matching and nonmatching fMRI locations were demonstrated qualitatively using four different sets of fMRI locations. First, the fMRI activity was assumed to be at the locations of the MEG sources (4,5) and (9,6) (Fig. 2C). In the second case, the fMRI was in two (false-positive) locations (2,3)

and (10,2) far from the MEG sources (shaded squares in Fig. 2D). In the third and fourth sets, the fMRI were close to the MEG locations but displaced either laterally (3,5) and (9,5) (Fig. 2D) or in the direction of the dipole moment vector (4,6) and (10,6) (Fig. 2F). For this simulation, Gaussian noise with zero mean and

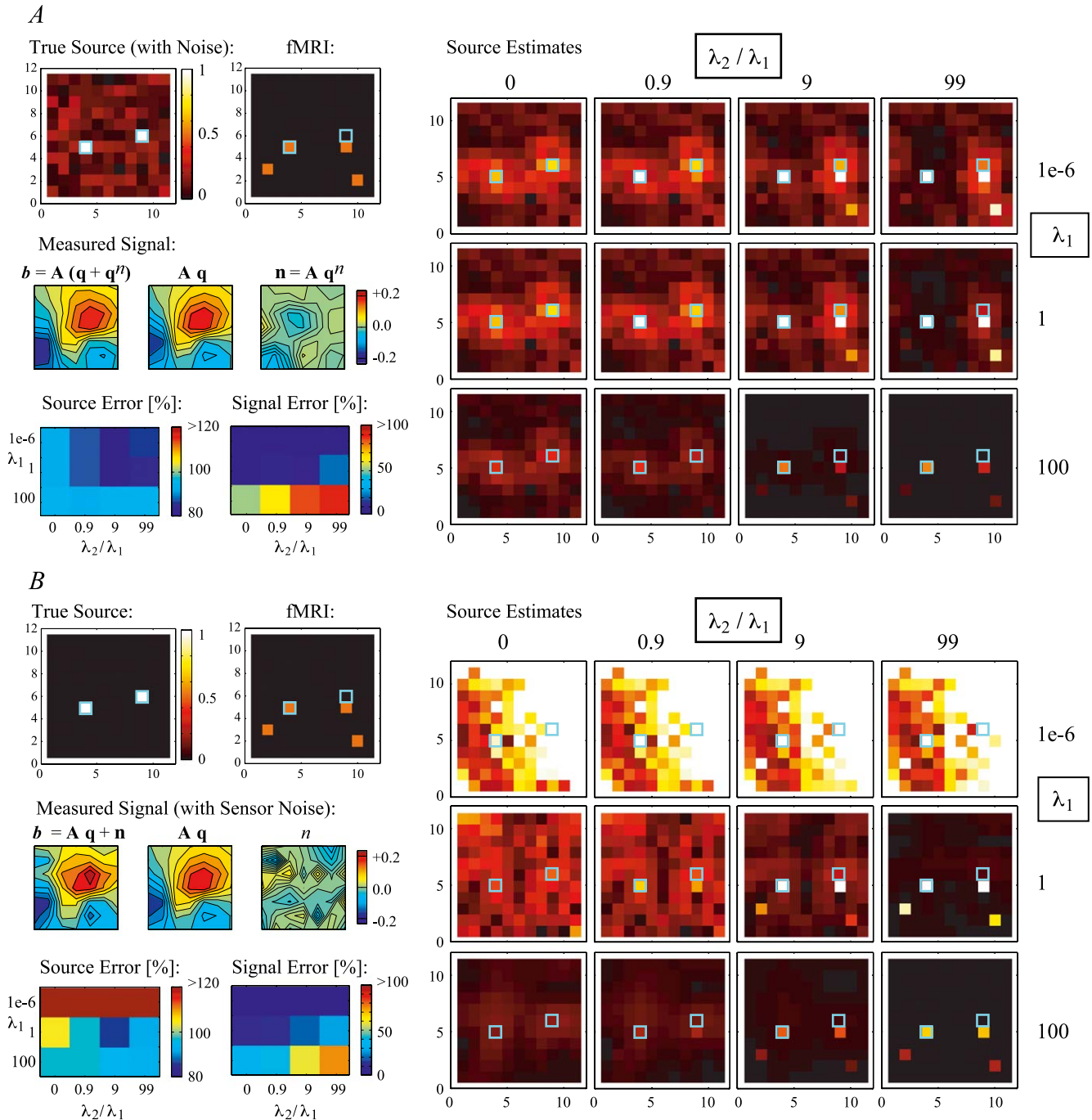


Fig. 3. Effect of the regularization parameters λ_1 and λ_2 on the fMRI-guided MEG source estimate. (A) Simulation with MEG source noise; all noise in the MEG signals originated from random dipoles within the source space. Top left: the simulated pattern of (true) MEG sources and fMRI locations. Middle left: the field pattern generated by the two MEG dipoles, without noise (b), with additive noise ($b + n$), and their difference (n). Top right: sub-space-regularized source estimates for different values of λ_1 ($1e - 6$, 1, 100) and λ_2 (0, 0.9 λ_1 , 9 λ_1 , 99 λ_1). The rows and columns correspond to different values of λ_1 and λ_2 , respectively. The magnitude of the estimated dipole moment at each location is indicated by color coding. The locations of the true MEG sources were the same as in Fig. 2 (indicated here by blue squares). Bottom left: relative error between the true and the estimated MEG source distribution (“source error”), as well as the relative error in the modeled signal values (“signal error”) for the different combinations of the regularization parameter values. (B) Simulation with independent sensor noise only.

standard deviation of 5% of the maximum measured signal was added; the explicit formula for \mathbf{q}^{SSR} (Eq. (13)) was used, with the regularization parameter $\lambda = 0.05$ for computing the MNE.

To illustrate the effect of the choice of the regularization parameters on the estimates, a set of solutions was computed using Eqs. (9) and (10), in which λ_1 and λ_2 were systematically varied ($\lambda_1 = 1e - 6, 1, 100$ and $\lambda_2 = 0.9 \lambda_1, 0.9 \lambda_1, 9 \lambda_1, 99 \lambda_1$). Note that λ_1 and λ_2 have physical units (inverse square of source current), whereas the ratio λ_2/λ_1 is dimensionless. The source configuration was the same as above, but here the sparse sensor grid (7×7) was used; four fMRI locations were assumed: one correct (5,4), one slightly displaced (5,0), and two faraway false-positives (3,2) and (2,10). For these simulations, two types of noise were used: (a) random normally distributed (SD σ_q) source current added to each source dipole element (“brain noise,” representing electrical “background” activity in the brain, which often dominates in MEG data) and (b) random normally distributed (SD σ_n) additive noise in the measured signals (“sensor noise,” representative of instrumentation noise, for example, SQUID noise or amplifier noise). The sensor noise was assumed independent between sensors, the source covariance matrix being $\mathbf{C}_1 = \sigma_q^2 \mathbf{I}$. For source noise, the noise covariance matrix was $\mathbf{C}_2 = \sigma_q^2 \mathbf{A} \mathbf{A}^T$. The sensor noise was equated with the source noise by requiring that $\text{Tr}(\mathbf{C}_1) = \text{Tr}(\mathbf{C}_2)$, resulting in $\sigma_n^2 = \sigma_q^2 \text{Tr}(\mathbf{A} \mathbf{A}^T) / m$; Tr indicates the sum of the diagonal elements of a matrix, and m is the number of sensors. In our simulations, we used $\sigma_q = 0.1$, which is 2.5% of the amplitude of the two dipoles of interest. The corresponding sensor noise was $\sigma_n = 0.026$, and the mean signal-to-noise ratio $\text{SNR} = \mathbf{b}^T \mathbf{b} / (m \sigma_n^2) \sim 14$.

Results

In the simulations, the location and spread of estimated source currents given by the SSR method were compared with those of the MNE. The MNE was a referent, which did not take fMRI information into account (Fig. 2B). The maximum source amplitudes in the MNE occurred at the locations of the true sources; however, the estimated source distribution is dispersed. This spread is characteristic to MNE, in general. The degree of smoothing in the spatial distribution in the MNE depends on the regularization; for examples, see Ahlfors et al. (1992).

We first evaluated the fMRI-guided inverse solution (Eq. (13)) in the favorable case in which the fMRI locations matched the true MEG source locations (Fig. 2C). The fMRI-guided solution is more confined to the correct source location compared with the MNE. Note that the modeled field pattern is identical for the MNE and \mathbf{q}^{SSR} (insets at upper right in Figs. 2B and C) because \mathbf{q}^{SSR} was defined in this case as a sum of the MNE and a source that does not generate a signal in the sensor array. In the second case, when the fMRI locations were far from the true MEG sources, they had little effect on the estimate, which resembled the MNE (Fig. 2D). In the third and fourth cases, we examined the effect of a simultaneous false-positive close to (10 mm) a false-negative fMRI (Figs. 2E and F). Even in this “worst case” scenario, the fMRI-guided solution was found to perform well, being able to “ignore” the incorrect fMRI prior. The solution was more biased towards the incorrect location when that location was in the direction parallel to the dipole moment (Fig. 2F) compared with a laterally displaced fMRI location (Fig. 2E).

The effect of varying the values of the two regularization parameters, λ_1 and λ_2 , on the inverse solution is depicted in Fig.

3. Fig. 3A shows a case with simulated “brain noise”—all the noise originated from random sources in the source space. Source estimates as a function of λ_1 and λ_2 are shown, as well as the corresponding relative source estimation error $\|\mathbf{q}^{\text{SSR}} - \mathbf{q}\|^2 / \|\mathbf{q}\|^2$ and the error in the modeled signals $\|\mathbf{b}^{\text{SSR}} - \mathbf{b}\|^2 / \|\mathbf{b}\|^2$, where $\mathbf{b}^{\text{SSR}} = \mathbf{A} \mathbf{q}^{\text{SSR}}$. The first regularization parameter λ_1 affects the smoothness of the estimates; for $\lambda_1 = 100$, most details disappeared.

When λ_2 increased, the estimate became more concentrated to the locations of the fMRI activity. Of the examples shown in Fig. 3A, the intermediate values $\lambda_1 = 1$ and $\lambda_2 / \lambda_1 = 9$ resulted in the smallest error in the source distribution (dark blue in “source errors” in Fig. 3A). Qualitatively, this solution gave a good estimate for the MEG source that matched the fMRI, although the false-positive fMRI locations showed activity as well. On the other hand, for the smaller value of $\lambda_2 / \lambda_1 = 0.9$, although less focal, the estimate was more concentrated on the correct location.

Fig. 3B shows a simulation in which random sensor noise was added to the measured signals (“sensor noise”). In this case, the spatial pattern of noise in the measured signals was less smooth than that in Fig. 3A. The MNE became unstable with very small values of λ_1 . The inverse estimates for $\lambda_2 = 0$ were without fMRI bias. The three values of λ_1 illustrate the main effect of regularization. For the very small value of $\lambda_1 = 10^{-6}$ (i.e., practically not regularized at all), the solution became unstable as it modeled also the random sensor noise; the corresponding estimation error in source space became very large, whereas the signal error was small. Again, the smallest estimation error in the source distribution occurred at intermediate values of λ_1 and λ_2 .

Discussion

We presented a novel interpretation of fMRI-guided MEG source estimation in terms of SSR. Simulated examples illustrated source estimates displaying reasonable and relevant patterns. Several factors, however, affect the results, including the properties of noise, the choice of the regularization parameters, and the match between fMRI locations and the MEG sources. It may be difficult to find optimal values that would work well for all simultaneous sources with this or any other method. However, the SSR formulation provides a principled way to approach the problem of incorporating fMRI priors into MEG source estimates.

Subspace regularization: fMRI-based bias on locations but not on amplitudes

In the subspace formulation, the fMRI prior does not assume preferred amplitudes for the MEG sources. This property of having bias on spatial locations only is well suited for the MEG inverse problem since there appears to be no simple relation between the hemodynamic response and electrophysiologic activity. The distance to the fMRI-defined subspace provides a measure for the compatibility of MEG source distributions and fMRI data. This provides an alternative interpretation of the fMRI-weighting parameter incorporated in the source covariance matrix (Liu et al., 1998) (see Appendix A) and complements probabilistic approaches to the problem (Baillet and Garnero, 1997; Clarke, 1989; Phillips et al., 2002a; Schmidt et al., 1999).

Further terms can be included in the cost function (Eq. (5)) to provide different preferences upon the set of solutions that otherwise are equally good from the point of view of the measured

MEG data; in depth-weighted MNE, deep sources are preferred to superficial ones using a weighting function (Ioannides, 1993); in LORETA, maximally smooth source distributions are preferred (Pascual-Marqui et al., 1994); and in FOCUSS, focal solutions are selected (Gorodnitsky et al., 1995). Other types of additional information that may turn out to be useful in the MEG source modeling include the expected (or maximum) magnitude of source current density, correlation in activity across multiple regions, and temporal patterns of activity (Baillet and Garnero, 1997) derived, for example, from intracranial human or animal data. Unlike the spatial bias, however, most of these other priors do not allow the subspace formulation. These types of data will become increasingly available and significant through ongoing neurodatabase projects. These databases will serve as a resource for deriving relevant information, including probability distributions, for guiding inverse solutions.

The regularization parameter λ_1 in the cost function of Eq. (5) prevents the norm of the solution from becoming excessively large. Importantly, this restricts the amplification of noise in the inverse solution for those source distributions to which the sensor lead fields (rows of \mathbf{A}) are only weakly sensitive. Fig. 3B illustrated how, without proper regularization, random sensor noise could render the inverse solution meaningless. Because the lead fields are relatively smooth and widely overlapping, it is often impossible to find spatial patterns of sources with physiologically reasonable amplitudes that would explain the measurement noise. On the other hand, when the measurement noise consisted patterns generated by noise sources in the brain, the measurement noise could be explained by “reasonable” source current patterns, and there was less need of regularization (Fig. 3A).

In principle, the regularization parameters should be adjusted such that the error in the explanation of the measured signals $\|\mathbf{b} - \mathbf{A}\mathbf{q}\|^2$ matches the estimated noise level. Various techniques have been suggested to determine the optimal value of the regularization parameter, including cross validation (Golub et al., 1979) and the L-curve method (Hansen, 1992). In an iterative restricted maximum likelihood (ReML) method, the conditional expectation of the source distribution and the regularization parameters are estimated jointly (Phillips et al., 2002b). It is important to avoid overfitting the data (too small λ); otherwise, noise may dominate the results. Typically, the results are less sensitive to too large values of the regularization parameter; however, spatial details in the source estimates can be lost, and the center of distributed estimates may shift towards deeper locations (Fuchs et al., 1999).

The second regularization parameter, λ_2 , controls the amount of bias towards the fMRI subspace. A high value of λ_2/λ_1 would force the solution to be close to the fMRI subspace. In the simulations, a “medium” value of λ_2 resulted in the desired effect of more focused solutions at the site of fMRI. However, if λ_2 is too large, the inverse solution tries to explain the measured data by putting large amplitudes in the fMRI locations, also those that do not correspond to true MEG sources. Ideally, a proper balance with λ_1 and λ_2 should be found such that the inverse solution is focused only at the sites of matching fMRI and MEG activity.

Nonmatching locations of fMRI and MEG activation

The SSR method has the desirable property of giving improved results when the prior information is compatible with the actual source distribution while being insensitive to incompatible priors (Vauhkonen et al., 1998). We found this in our simulations as

well—the method performed well even in situations with simultaneous false-positive and false-negative fMRI locations. In terms of constrained optimization, it is the MEG data that define the constraint; therefore, we prefer the expression “fMRI-guided” (as opposed to “fMRI-constrained”) MEG inverse solution. In particular, Eq. (13) was derived using the assumption that the model reproduces the MEG data exactly (i.e., the solution belongs to the set M).

It is reasonable to expect mismatches between locations of fMRI activation and MEG sources. False-positive fMRI locations are bound to occur in practice due to the limited spatial sensitivity patterns of MEG sensors and the limited time resolution of fMRI. Some source activity may be located or oriented such that there is little magnetic field outside the head. Examples of this are radially oriented sources, deep sources, or “closed field” sources for which the activity patterns are such that the total macroscopic current cancels out. All of these could generate significant signal in fMRI but not in MEG. Furthermore, typically only some of the MEG sources are active at a given time instant, whereas fMRI pools activity over time. This results in missing MEG sources for inverse solutions that are computed independently at each time instant (as in our simulations). Thus, fMRI and MEG may coincide at some time points, whereas there may be a missing MEG source at other times. In our simulations, isolated false-positive fMRI had little effect on the fMRI-guided source estimates.

Missing (false-negative) fMRI can occur due to artifactual lack of fMRI activity (e.g., susceptibility artifacts or a partial-only coverage of the brain volume) or to differences in the referent or baseline condition, particularly with blocked designs. While event-related fMRI can equate fMRI and MEG designs and baselines qualitatively, the relative amounts of summation in the baseline or referent for fMRI may be different than with MEG. Thus, weak signals that may rise above noise in MEG may fail to be significant in event-related fMRI. False-negatives may also arise from differences in the physiologic origin of the hemodynamic and electrophysiologic measures. Simple false-negative fMRI appeared to have little effect, with the inverse solution resembling the MNE (Babiloni et al. 2003).

The occurrence of simultaneous false-positive and false-negative fMRI loci is reasonably expected. For example, an MEG source in visual cortex may be active for the first part of a 1000-ms period following a stimulus and then return to baseline levels for the latter part of the period. The active and inactive periods can be detected with the MEG; however, the fMRI counterpart cannot differentiate between the two periods. Thus, the fMRI activity will constitute a false-positive with respect to the latter period. Now consider how an fMRI false-negative in a neighboring area may also readily arise. A brief (e.g., 100 ms) electrophysiologic activation could occur in a neighboring area that would be detected by MEG but might not generate a sufficiently large hemodynamic response to be detected with fMRI. As a result, there would be both false-positive and false-negative fMRI loci near each other. This and other scenarios for simultaneous false-positive and false-negative fMRI are likely to occur in cognitive experiments.

Here, the fMRI data were assumed to be thresholded—each volume element was either active or not active. Typically, the results of fMRI data analysis are statistical parametric maps, that is, a significance value is assigned to each volume element. Further work is required to establish how to optimize the significance

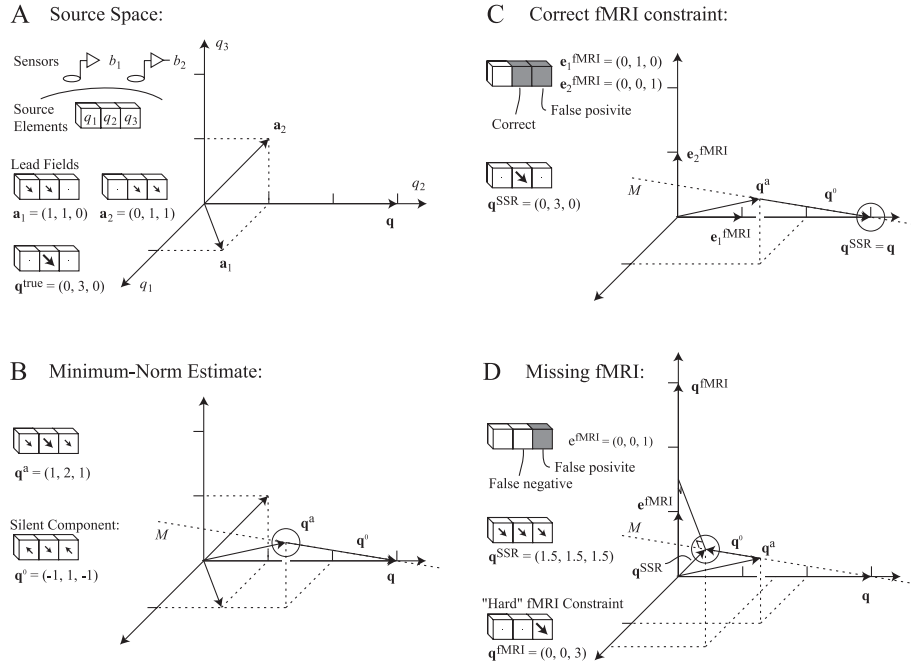


Fig. 4. An example of source estimates as vectors in the source space. (A) The source space consists three source elements. The lead fields of the two sensors are also vectors in this space. The arrows indicate the direction and magnitude of the elements of source space vectors. (B) The minimum norm estimate (circle) is at the intersection of M and the plane (not depicted) defined by the lead field vectors. (C) Sub-space-regularized estimate (circle) with a correct fMRI constrained. The sites of fMRI activity are indicated with shading. (D) The effect of incorrect fMRI on the source estimates.

threshold used for the selection of volume elements to define the subspace S^{fMRI} . A high threshold may result in missing fMRI locations, whereas a low threshold reduces the specificity and thus the usefulness of the fMRI information in constraining the MEG source locations. The two extreme cases, no fMRI (S^{fMRI} is empty or belongs completely to S^0 , the subspace invisible to MEG) and all fMRIs (S^{fMRI} equals the whole source space or includes the MEG-visible subspace S^v) will give the same result, that is, the MNE. Somewhere in-between, there should be an optimal value for the fMRI significance threshold for the MEG analysis. It may also be possible to construct a distance measure in which the significance values of fMRI activation are explicitly taken into account.

Our approach addresses the problem of using information from fMRI to guide the MEG source analysis. In principle, multimodal imaging provides the possibility of considering also the reverse question: Can MEG data be used to guide fMRI analysis? For example, the significance values for statistical test of fMRI activation could be adjusted on the basis of prior information from MEG. The Bayesian approach appears to provide a natural framework for this type of analysis (e.g., see Friston et al., 2002).

In conclusion, the SSR formulation and its geometric interpretation can provide useful insights to the problem of how to use information from fMRI/PET when determining the sources of MEG/EEG signals.

Acknowledgments

This work was supported by Whitaker foundation grant RG-01-0294, by NIH grants NS27900, DA09972, and MH-DA52176 (Human Brain Project), and by the Human Frontiers Science

Program. This work was supported in part by The National Center for Research Resources (P41RR14075) and the Mental Illness and Neuroscience Discovery (MIND) Institute. We thank Drs. John Foxe, Dirk Heslenfeld, Jan Hrabec, Kevin Knuth, Cliff Saron, and Michael Worden for constructive discussions and suggestions.

Appendix A. Comparison with the method of Liu et al. (1998)

In this Appendix, we derive the relationship between the two regularization parameters of the SSR method and the parameters used by Liu et al. (1998). In their method, fMRI is taken into account in the diagonal elements of the a priori source covariance matrix $\mathbf{R} = \beta \text{diag}(\sigma_i^2)$ in Eq. (5); $\sigma_i^2 = 1$ for fMRI locations and $\sigma_i^2 = \alpha \leq 1$ for non-fMRI locations; β is a scaling factor related to the square of the expected source amplitude. There is a trade-off between strong fMRI weighting (small α), which may lead to mislocation of source activity when fMRI and MEG do not match, and weak weighting (large α), which lessens the impact of fMRI information on the inverse solution. Based on extensive Monte Carlo stimulations on a realistic head model, Liu et al. (1998) suggested that $\alpha = 0.1$, corresponding to 90% fMRI weighting, gives good results.

Using the notation of Eq. (7), the source covariance matrix can be written as

$$\mathbf{R} = \beta \text{diag}[(1 - \delta_i)\alpha + \delta_i],$$

where $\delta_i = 1$ for fMRI loci and 0 otherwise. The SSR and the method of Liu et al. (1998) are mathematically equivalent if

$$\beta^{-1} \text{diag}[(1 - \delta_i)\alpha + \delta_i]^{-1} = \text{diag}[\lambda_1 + \lambda_2(1 - \delta_i)].$$

Solving for λ_1 and λ_2 , we get

$$\lambda_1 = \beta^{-1}$$

$$\lambda_2 = \beta^{-1}(\alpha^{-1} - 1)$$

or conversely

$$\beta = \lambda_1^{-1}$$

$$\alpha = \lambda_1/(\lambda_1 - \lambda_2)$$

Thus, there is a relatively simple relationship between the regularization parameters λ_1 and the parameters β and α of Liu et al. (1998). When there is no fMRI information, λ_1 (or β) is the only regularization parameter (i.e., $\lambda_2 = 0$, $\alpha = 1$). If $\alpha \geq 0$, then $\lambda_2 \geq \infty$, which corresponds to the hard fMRI constraint; that is, only the fMRI locations are relevant to the solution. The values $\alpha = 0.1$ and $\alpha = 0.01$ correspond to the SSR regularization parameter values $\lambda_2 = 9 \lambda_1$ and $\lambda_2 = 99 \lambda_1$, respectively.

Appendix B. An example with three sources and two sensors

The geometric interpretation of the fMRI-guided MEG inverse solution is illustrated by a simple example, which can be easily visualized and solved analytically. Assume a source space of three elements, $(q_1, q_2, q_3)^T$, and two sensors with lead fields, $\mathbf{a}_1 = (1, 1, 0)^T$ and $\mathbf{a}_2 = (0, 1, 1)^T$ (Fig. 4A). The problem is underdetermined, which is typical of the MEG inverse problem.

Minimum norm estimate (Fig. 4B): Let the true source current distribution be $\mathbf{q} = (0, 3, 0)^T$ and the measured signals $\mathbf{b} = (3, 3)^T$. The vector $\mathbf{q}^a = (1, 2, 1)^T$ is the point closest to the true source in the plane S^a defined by the lead field vectors \mathbf{a}_1 and \mathbf{a}_2 ; in this noiseless case, \mathbf{q}^a is also the MNE. The difference $\mathbf{q}^0 = \mathbf{q} - \mathbf{q}^a = (-1, 1, -1)^T$ is orthogonal to that plane (the silent component). The set M of all solutions compatible with the MEG is $(1, 2, 1)^T + c(-1, 1, -1)^T$, where c is a real number.

Source estimate guided by correct fMRI (Fig. 4C): Assuming that fMRI showed activity in the second and third elements, thus the subspace S^{fMRI} is spanned by vectors $(0, 1, 0)^T$ [correct] and $(0, 0, 1)^T$ [missing MEG source]; there are no missing fMRI. The fMRI-guided solution is found by choosing \mathbf{q}^{SSR} such that it intersects the $q_2 q_3$ plane. Thus, $\mathbf{q}^{\text{SSR}} = (1, 2, 1)^T + 1(-1, 1, -1)^T = (0, 3, 0)^T$, which is exactly the source distribution. In matrix notation, $\mathbf{P} = \text{diag}(1, 0, 0)$, $\mathbf{D} = 3^{-1/2}(-1, 1, -1)^T$, $\mathbf{D}^T \mathbf{P} \mathbf{D} = 1/3$, and $(\mathbf{D}^T \mathbf{P} \mathbf{D})^\dagger = 3$, in Eq. (13).

Missing fMRI (Fig. 4D): Next we consider the case that the fMRI showed activity only in the third (incorrect) element and not in the second where the MEG activity was. Thus, S^{fMRI} is now one dimensional, spanned by $(0, 0, 1)^T$. We select the parameter c such that \mathbf{q}^{SSR} is as close to S^{fMRI} as possible: $[(2+c)^2 + (1-c)^2]$. The result is $\mathbf{q}^{\text{SSR}} = (1, 2, 1)^T - (1/2)(-1, 1, -1)^T = (1.5, 1.5, 1.5)^T$. In matrix notation, $\mathbf{P} = \text{diag}(1, 1, 0)$ and $(\mathbf{D}^T \mathbf{P} \mathbf{D})^\dagger = 3/2$. The SSR solution is further from the true source than is \mathbf{q}^{MNE} . The fMRI information modifies the solution by adding a silent component to make the estimate better compatible with the fMRI. In this case, no estimate is compatible with both MEG and fMRI because S^{fMRI} and M do not intersect. A strict fMRI constraint would result in the solution $(0, 0, 3)^T$. The missing fMRI is identifiable because the MEG data are not compatible with the fMRI constraint. Note that

an fMRI pattern consisting both q_1 and q_3 , but not (the correct MEG source) q_2 , would contain a nonidentifiable missing fMRI because the solution $\mathbf{q}^{\text{fMRI}} = (3, 0, 3)^T$ is consistent with the MEG data (not shown).

References

- Ahlfors, S.P., Ilmoniemi, R.J., Hämmäläinen, M.S., 1992. Estimates of visually evoked cortical currents. *Electroencephalogr. Clin. Neurophysiol.* 82, 225–236.
- Ahlfors, S.P., Simpson, G.V., Dale, A.M., Belliveau, J.W., Liu, A.K., Korvenoja, A., Virtanen, J., Huutilainen, M., Tootell, R.B., Aronen, H.J., Ilmoniemi, R.J., 1999. Spatiotemporal activity of a cortical network for processing visual motion revealed by MEG and fMRI. *J. Neurophysiol.* 82, 2545–2555.
- Babiloni, F., Babiloni, C., Carducci, F., Romani, G.L., Rossini, P.M., Angelone, L.M., Cincotti, F., 2003. Multimodal integration of high-resolution EEG and functional magnetic resonance imaging data: a simulation study. *NeuroImage* 19, 1–15.
- Backus, G.E., 1971. Inference from inadequate and inaccurate data. In: Reid, W.H. (Ed.), *Mathematical Problems in the Geophysical Sciences 2. Inverse Problems, Dynamo Theory, and Tides*. American Mathematical Society, Providence, RI, pp. 1–105.
- Baillet, S., Garnero, L., 1997. A Bayesian approach to introducing anatomic-functional priors in the EEG/MEG inverse problem. *IEEE Trans. Biomed. Eng.* 44, 374–385.
- Beisteiner, R., Erdler, M., Teichtmeister, C., Diemling, M., Moser, E., Edward, V., Deecke, L., 1997. Magnetoencephalography may help to improve functional MRI brain mapping. *Eur. J. Neurosci.* 9, 1072–1077.
- Clarke, C.J.S., 1989. Probabilistic methods in a biomagnetic inverse problem. *Inverse Problems* 5, 999–1012.
- Cohen, D., Halgren, E., 2003. Magnetoencephalography (neuromagnetism). In: Adelman, G., Smith, B.H. (Eds.), *Encyclopedia of Neuroscience*. Elsevier, Amsterdam. In press.
- Cuffin, B.N., Cohen, D., 1979. Comparison of the magnetoencephalogram and electroencephalogram. *Electroencephalogr. Clin. Neurophysiol.* 47, 132–146.
- Dale, A.M., Sereno, M.I., 1993. Improved localization of cortical activity by combining EEG and MEG with MRI cortical surface reconstruction: a linear approach. *J. Cogn. Neurosci.* 5, 162–176.
- Dale, A.M., Liu, A.K., Fischl, B.R., Buckner, R.L., Belliveau, J.W., Lewine, J.D., Halgren, E., 2000. Dynamic statistical parametric mapping: combining fMRI and MEG for high-resolution imaging of cortical activity. *Neuron* 26, 55–67.
- Devor, A., Dunn, A.K., Andermann, M.L., Ulbert, I., Boas, D.A., Dale, A.M., 2003. Coupling of total hemoglobin concentration, oxygenation, and neural activity in rat somatosensory cortex. *Neuron* 39, 353–359.
- FitzGerald, D.B., Cosgrove, G.R., Ronner, S., Jiang, H., Buchbinder, B.R., Belliveau, J.W., Rosen, B.R., Benson, R.R., 1997. Location of language in the cortex: a comparison between functional MR imaging and electrocortical stimulation. *AJNR Am. J. Neuroradiol.* 18, 1529–1539.
- Friston, K.J., Penny, W., Phillips, C., Kiebel, S., Hinton, G., Ashburner, J., 2002. Classical and Bayesian inference in neuroimaging: theory. *NeuroImage* 16, 465–483.
- Fuchs, M., Wagner, M., Kohler, T., Wischmann, H.A., 1999. Linear and nonlinear current density reconstructions. *J. Clin. Neurophysiol.* 16, 267–295.
- George, J.S., Lewis, P.S., Ranken, D.M., Kaplan, L., Wood, C.C., 1991. Anatomical constraints for neuromagnetic source models. *SPIE Medical Imaging V: Image Physics*, vol. 1443. SPIE, Bellingham, WA, pp. 37–51.
- George, J.S., Aine, C.J., Mosher, J.C., Schmidt, D.M., Ranken, D.M., Schlitt, H.A., Wood, C.C., Lewine, J.D., Sanders, J.A., Belliveau, J.W., 1995. Mapping function in the human brain with magnetoencephalography, anatomical magnetic resonance imaging, and functional magnetic resonance imaging. *J. Clin. Neurophysiol.* 12, 406–431.

- Gevins, A., Leong, H., Smith, M.E., Le, J., Du, R., 1995. Mapping cognitive brain function with modern high-resolution electroencephalography. *Trends Neurosci.* 18, 429–436.
- Glaser, E.M., Ruchkin, D.S., 1976. *Principles of Neurobiological Signal Analysis*. Academic Press, New York.
- Golub, G.H., Heath, M., Wahba, G., 1979. Generalized cross-validation as a method for choosing a good ridge parameter. *Technometrics* 21, 215–223.
- Gorodnitsky, I.F., George, J.S., Rao, B.D., 1995. Neuromagnetic source imaging with FOCUSS: a recursive weighted minimum norm algorithm. *Electroencephalogr. Clin. Neurophysiol.* 95, 231–251.
- Grave de Peralta Menendez, R., Hauk, O., Andino, S.G., Vogt, H., Michel, C., 1997. Linear inverse solutions with optimal resolution kernels applied to electromagnetic tomography. *Hum. Brain Mapp.* 5, 454–467.
- Greenblatt, R.E., 1993. Probabilistic reconstruction of multiple sources in the bioelectromagnetic inverse problem. *Inverse Problems* 9, 271–284.
- Hämäläinen, M.S., Ilmoniemi, R.J., 1984. Interpreting measured magnetic fields of the brain: estimates of current distributions. Technical Report TKK-F-A559. Helsinki University of Technology, Otaniemi, Finland, pp. 1–35.
- Hämäläinen, M.S., Ilmoniemi, R.J., 1994. Interpreting magnetic fields of the brain: minimum norm estimates. *Med. Biol. Eng. Comput.* 32, 35–42.
- Hämäläinen, M., Hari, R., Ilmoniemi, R.J., Knuutila, J., Lounasmaa, O.V., 1993. Magnetoencephalography—Theory, instrumentation, and applications to noninvasive studies of the working human brain. *Rev. Mod. Phys.* 65, 413–497.
- Hansen, P.C., 1992. Analysis of discrete ill-posed problems by the means of the L-curve. *SIAM Rev.* 34, 561–580.
- Heinze, H.J., Mangun, G.R., Burchert, W., Hinrichs, H., Scholz, M., Munte, T.F., Gos, A., Scherg, M., Johannes, S., Hundeshagen, H., et al., 1994. Combined spatial and temporal imaging of brain activity during visual selective attention in humans. *Nature* 372, 543–546.
- Helmholtz, H., 1853. Ueber einige Gesetze der Vertheilung elektrischer Ströme in körperlichen Leitern, mit Anwendung auf die thierisch-elektrischen Versuche. *Ann. Phys. Chem.* 89, 211–233, 353–377.
- Ioannides, A.A., 1993. Brain function as revealed by current density analysis of magnetoencephalography signals. *Physiol. Meas.* 14 (Suppl. 4A), A75–A80.
- Jeffs, B., Leahy, R., Singh, M., 1987. An evaluation of methods for neuromagnetic image reconstruction. *IEEE Trans. Biomed. Eng.* 34, 713–723.
- Karjalainen, P.A., Kaipio, J.P., Koistinen, A.S., Vauhkonen, M., 1999. Subspace regularization method for the single-trial estimation of evoked potentials. *IEEE Trans. Biomed. Eng.* 46, 849–860.
- Korvenoja, A., Huttunen, J., Salli, E., Pohjonen, H., Martinkauppi, S., Palva, J.M., Lauronen, L., Virtanen, J., Ilmoniemi, R.J., Aronen, H.J., 1999. Activation of multiple cortical areas in response to somatosensory stimulation: combined magnetoencephalographic and functional magnetic resonance imaging. *Hum. Brain Mapp.* 8, 13–27.
- Liu, A.K., Belliveau, J.W., Dale, A.M., 1998. Spatiotemporal imaging of human brain activity using functional MRI constrained magnetoencephalography data: Monte Carlo simulations. *Proc. Natl. Acad. Sci. U.S.A.* 95, 8945–8950.
- Liu, A.K., Dale, A.M., Belliveau, J.W., 2002. Monte Carlo simulation studies of EEG and MEG localization accuracy. *Hum. Brain Mapp.* 16, 47–62.
- Logothetis, N.K., 2003. The underpinnings of the BOLD functional magnetic resonance imaging signal. *J. Neurosci.* 23, 3963–3971.
- Malonek, D., Grinvald, A., 1996. Interactions between electrical activity and cortical microcirculation revealed by imaging spectroscopy: implications for functional brain mapping. *Science* 272, 551–554.
- Menon, V., Ford, J.M., Lim, K.O., Glover, G.H., Pfefferbaum, A., 1997. Combined event-related fMRI and EEG evidence for temporal–parietal cortex activation during target detection. *NeuroReport* 8, 3029–3037.
- Morioka, T., Yamamoto, T., Mizushima, A., Tombimatsu, S., Shigetou, H., Hasuo, K., Nishio, S., Fujii, K., Fukui, M., 1995. Comparison of magnetoencephalography, functional MRI, and motor evoked potentials in the localization of the sensory–motor cortex. *Neurol. Res.* 17, 361–367.
- Mosher, J.C., Lewis, P.S., Leahy, R.M., 1992. Multiple dipole modeling and localization from spatio-temporal MEG data. *IEEE Trans. Biomed. Eng.* 39, 541–557.
- Pascual-Marqui, R.D., Michel, C.M., Lehmann, D., 1994. Low resolution electromagnetic tomography: a new method for localizing electrical activity in the brain. *Int. J. Psychophysiol.* 18, 49–65.
- Phillips, C., Rugg, M.D., Friston, K.J., 2002a. Anatomically informed basis functions for EEG source localization: combining functional and anatomical constraints. *NeuroImage* 16, 678–695.
- Phillips, C., Rugg, M.D., Friston, K.J., 2002b. Systematic regularization of linear inverse solutions of the EEG source localization problem. *NeuroImage* 17, 287–301.
- Puce, A., 1995. Comparative assessment of sensorimotor function using functional magnetic resonance imaging and electrophysiological methods. *J. Clin. Neurophysiol.* 12, 450–459.
- Sanders, J.A., Lewine, J.D., Orrison, W.W., 1996. Comparison of primary motor cortex localization using functional magnetic resonance imaging and magnetoencephalography. *Hum. Brain Mapp.* 4, 47–57.
- Scherg, M., Von Cramon, D., 1986. Evoked dipole source potentials of the human auditory cortex. *Electroencephalogr. Clin. Neurophysiol.* 65, 344–360.
- Schmidt, D.M., George, J.S., Wood, C.C., 1999. Bayesian inference applied to the electromagnetic inverse problem. *Hum. Brain Mapp.* 7, 195–212.
- Sekihara, K., Scholz, B., 1996. Generalized Wiener estimation of three-dimensional current distribution from biomagnetic measurements. *IEEE Trans. Biomed. Eng.* 43, 281–291.
- Simpson, G.V., Belliveau, J.W., Foxe, J.J., Baker, J.R., Vaughan, H.G., 1993. Spatial imaging and temporal dynamics of visual brain activation through integration of electrophysiological (ERP) and hemodynamic (fMRI) measures. *Soc. Neurosci. Abstr.* 19, 1604.
- Simpson, G.V., Pflieger, M.E., Foxe, J.J., Ahlfors, S.P., Vaughan Jr., H.G., Hrabe, J., Ilmoniemi, R.J., Lantos, G., 1995. Dynamic neuroimaging of brain function. *J. Clin. Neurophysiol.* 12, 432–449.
- Smith, W.E., Dallas, W.J., Kullman, W.H., Schliitt, H.A., 1990. Linear estimation theory applied to the reconstruction of a 3-D vector current distribution. *Appl. Opt.* 29, 658–667.
- Snyder, A.Z., Abdullaev, Y.G., Posner, M.I., Raichle, M.E., 1995. Scalp electrical potentials reflect regional cerebral blood flow responses during processing of written words. *Proc. Natl. Acad. Sci. U.S.A.* 92, 1689–1693.
- Tarantola, A., 1987. *Inverse Problem Theory. Methods for Data Fitting and Model Parameter Estimation*. Elsevier, Amsterdam.
- Tesche, C.D., Uusitalo, M.A., Ilmoniemi, R.J., Huotilainen, M., Kajola, M., Salonen, O., 1995. Signal-space projections of MEG data characterize both distributed and well-localized neuronal sources. *Electroencephalogr. Clin. Neurophysiol.* 95, 189–200.
- Tikhonov, A.N., Arsenin, V.Y., 1977. *Solutions of Ill-Posed Problems*. Winston, Washington, DC.
- Uusitalo, M.A., Ilmoniemi, R.J., 1997. Signal-space projection method for separating MEG or EEG into components. *Med. Biol. Eng. Comput.* 35, 135–140.
- Vauhkonen, M., Vadasz, D., Karjalainen, P.A., Somersalo, E., Kaipio, J.P., 1998. Tikhonov regularization and prior information in electrical impedance tomography. *IEEE Trans. Med. Imag.* 17, 285–293.
- Wang, J.Z., Williamson, S.J., Kaufman, L., 1992. Magnetic source images determined by a lead-field analysis: the unique minimum-norm least-squares estimation. *IEEE Trans. Biomed. Eng.* 39, 665–675.
- Woldorff, M.G., Matzke, M., Zamarripa, F., Fox, P.T., 1999. Hemodynamic and electrophysiological study of the role of the anterior cingulate in target-related processing and selection for action. *Hum. Brain Mapp.* 8, 121–127.
- Worden, M., Vincent, D.J., Schneider, W., Shedden, J.M., 1996. Constraining high-density ERP source analysis using functional MRI. In: Witten, M., Vincent, D.J. (Eds.), *Building a Man in the Machine: Computational Medicine, Public Health, and Biotechnology: Part II*. World Scientific Press, Singapore, pp. 723–743.